Published in final edited form as:
J Biophotonics. 2013 June ; 6(0): . doi:10.1002/jbio.201200221.

Magnetomotive photoacoustic imaging: *in vitro* studies of magnetic trapping with simultaneous photoacoustic detection of rare circulating tumor cells

Chen-wei Wei[1], **Jinjun Xia**[1], **Ivan Pelivanov**[1,2], **Congxian Jia**[1], **Sheng-Wen Huang**[1], **Xiaoge Hu**[1], **Xiaohu Gao**[1], and **Matthew O'Donnell**[*,1]

[1]Department of Bioengineering, University of Washington, 3720, 15th AVE NE, Seattle, WA 98195, USA

[2]Physics Faculty of M.V. Lomonosov Moscow State University, Leninskie Gory, 1, bld.2, 119991, Moscow, Russia

Abstract

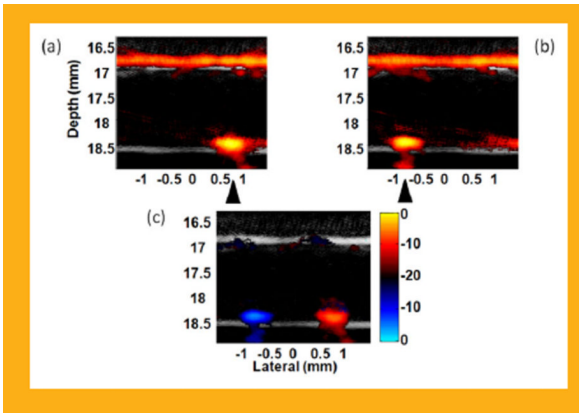

Photoacoustic (PA) imaging has been demonstrated to be a promising modality in molecular imaging for detection of nanoparticle-targeted diseased cells or tissues. However, intrinsic absorbers, such as blood, produce strong PA background signals that severely degrade the detection sensitivity and specificity of targeted objects. Magnetomotive photoacoustic (mmPA) imaging, a newly developed molecular imaging modality, introduced dynamic manipulation into traditional PA imaging. Unlike conventional PA imaging, magnetomotive manipulation with simultaneous ultrasound/PA imaging of agents incorporating magnetic nanoparticles enables direct visualization of the signal generating object and can dramatically reduce background signals from strong optical absorbers. This paper briefly reviews recent developments in mmPA imaging, including uses of composite contrast agent, design of magnet system, and data processing for motion filtering. The use of mmPA imaging in detecting rare circulating tumor cells in blood vessels, which remains a big challenge for real-time *in vivo* examination using current methodologies, was also addressed.

Fusion Images (ultrasound + photoacousitc) of manipulation of magnetic-gold nanorod contrast agent targeted polystyrene beads in ink solution flowing with a rate of 12 ml/min [1]. Images (a)

[*]Corresponding author: odonnel@uw.edu, Phone: 206-543-1829, FAX: 206-685-066.

Author biographies Please see Supporting Information online.

and (b) were acquired with a cone magnet array at two different positions, and (c) is the differential image of (a) and (b). A bipolar color scale is used to display the sign of the difference. Triangles indicate the magnet positions.

Keywords

photoacoustic imaging; ultrasound imaging; magnetic manipulation; magnetic nanoparticles; gold nanorods; composite contrast agent; contrast improvement

1. Introduction

Photoacoustic (PA) imaging combines optical probing of an object under study by short laser pulse irradiation with ultrasound (US) detection of the resultant thermally-induced acoustic waves [2–3]. The combination of high optical contrast enhanced by the specific optical absorption of contrast agents and sub-mm spatial resolution of US detection deep within tissue has made PA imaging a promising tool for molecular imaging [4–7]. PA imaging has great potential to detect and differentiate specific molecules from other components with a unique contrast mechanism, optical absorption. By targeting a designed contrast agent with absorption peak at a specific wavelength to biological objects, such as tumor cells, PA imaging can non-invasively image targeted objects specifically and sensitively [8–10].

Unfortunately, intrinsic absorbers, such as tissues and blood, are efficient sources of strong background PA signals, which seriously degrade the sensitivity of detecting targeted molecules or cells. Figure 1 presents an example of PA molecular imaging of a tumor in a living mouse [8]. After intravenous injection of a targeted contrast agent (Figure 1b), cyclic Arg-Gly-Asp (RGD) peptide-coupled carbon nanotubes, the PA signal in the tumor region significantly increases compared to the pre-injection image (Figure 1a), indicating the efficacy of targeted contrast agent recognition of the tumor region. However, non-negligible PA signals generated from the absorption of intrinsic tissues or blood are seen in the pre-injection image. This nonspecific signal decreases the sensitivity and makes quantitative measurement almost impossible, especially when diseased tissue approaches the resolution limit of the imaging system, as in a very early stage tumor where the number of cancer cells is small, or for rare circulating tumor cells (CTCs) in the vasculature.

Detection of CTCs represents a significant problem in molecular imaging and may be approached using new targeted nanosystems optimized for PA imaging if the strong PA background signal from blood can be suppressed. CTCs originate from a primary tumor and spread to different sites in the body through blood or lymphatics to develop metastasis, which causes over 90% of cancer deaths [11]. It remains a big challenge to detect CTCs because of their rarity. Their typical number for an active tumor is fewer than 10 cells per milliliter of blood [12]. Many techniques can separate and identify CTCs, including immunomagnetic enrichment to capture CTCs labeled with polymer or ferromagnetic beads coated via antibody-antigen binding from blood samples [13], microchips and microfluidic devices [14], filters with precise pore size allowing blood cells to pass but retaining CTCs [15], and flow cytometry to sort CTCs by centrifugation and staining identification [16]. Unfortunately, all these methods are used *in vitro*, not *in vivo*, so real-time readout is not possible for these methods [13]. Also, repeatedly taking samples by invasive biopsies and bone marrow aspirations is required, which increases patient pain. In particular, diagnostic confidence significantly decreases due to a limited sample volume (typically 5– 10 ml).

Recently, both optical [17] and PA imaging [18] have been proposed for non-invasive CTC detection. Because optical methods only work on superficial vessels, the blood volume interrogated in a reasonable procedure time (e.g., within 10 minutes) is prohibitively small for highly sensitive detection. In contrast, PA imaging can image peripheral vessels at depth, such as the radial and brachial arteries, providing access to a relatively large blood volume over the same procedure time. By targeting CTCs with functionalized contrast agents with an absorption peak at a fixed wavelength, targeted cells can be sensitively detected. Unfortunately, as mentioned earlier, blood itself is a very efficient optical absorber and creates strong PA background signals that can easily block the signals from targeted CTCs.

To increase contrast in PA molecular imaging of rare cell types (i.e., CTCs) above the intrinsic background absorption within tissues, an alternative contrast mechanism other than optical absorption can be used. A new contrast enhancement imaging technique to suppress background signals through magnetic accumulation and manipulation of objects labeled with magneto-sensitive contrast agent has been developed [1, 19–25]. This technique, called magnetomotive photoacoustic (mmPA) imaging, uses a composite contrast agent combining highly optically absorptive and magneto-sensitive components, enabling magnetic enrichment and photoacoustic detection of objects targeted with the contrast agent. By manipulating the objects, they can be differentiated from the magnetically-insensitive background by applying motion filters [1, 19–20, 24]. For CTC detection, mmPA imaging provides improved sensitivity over traditional PA imaging, exhibiting enormous advantage in detecting rare diseased cells in a heterogeneous background with strong scattering and absorption.

This paper briefly reviews the uses of composite contrast agents in mmPA imaging and data processing for background suppression in Section 2. In Section 3, current developments of mmPA imaging in detecting CTCs are reviewed, including a multiple wavelength approach with multiple contrast agents (Section 3.1), the specific type of composite contrast agent (Section 3.2) used for detecting CTCs, setup of the magnet and imaging systems, and *in vitro* experimental results using polystyrene beads (Section 3.3) and HeLa cells (Section 3.4) mimicking CTCs as imaging targets. The paper concludes in Section 4.

2. mmPA imaging: contrast enhancement with composite contrast agent

To enhance the specific contrast of a molecularly targeted agent for PA imaging, magnetic manipulation of composite nanoparticles combining a magnetic component with a commonly-used PA contrast agent has been investigated [19]. Figure 2 shows an example of a composite particle with a magnetic nanoparticle (MNP) core and a gold shell [19]. By controlling the shell thickness, the composite particles can have a broad optical absorption band with peak wavelength within the optical window in biological tissue (800–1000 nm), in which light has maximal penetration into tissues for biomedical imaging.

With the magnetic component, the composite contrast agent can be magnetically manipulated to create movement coherent with the magnetic field. Any static background (i.e., intrinsic tissue absorbers) or absorbers that move incoherently with the magnetic field (i.e., blood) can be largely suppressed. This idea of background suppression with mmPA imaging is shown in Figure 3 [19]. Composite particles move up/down when the magnetic field is turned on/off, due to gaining/losing the attractive force (Figure 3a). By biologically coupling the contrast agent to targeted tissues or cells, local movement in the region can be created with an external magnetic field. At the same time, the “shaking” process is continuously monitored with PA imaging. With full knowledge of the magnetic pattern, motion filtering can be applied to the series of recorded PA images to suppress all background signals insensitive to the magnetic field (Figure 3b).

The principle was first demonstrated in a phantom experiment with setup shown in Figure 4 [20]. Different particles, including pure gold nanorods (GNRs), MNPs, and composite particles, were made as inclusions in a polyvinyl alcohol (PVA) phantom immersed in a water tank. An electromagnet was placed under the tank to apply magnetic pulses controlled by a function generator. A laser source, an ultrasound transducer with a scanning motor, and the electromagnet were synchronized to record PA signals over a magnet cycle (off-on-off) at each scanning point.

An example of a data processing scheme to suppress magnetically insensitive background signals in mmPA imaging is illustrated in Figure 5 [19]. A series of PA images of three inclusions with different particles were acquired using the setup described in Figure 4. By applying a motion tracking algorithm, displacement of each pixel can be estimated as a function of record time. According to the displacement, a weighting image, which recognizes pixels that move coherently with the magnet field, can be created (Figure 5f). Figure 5g shows the result of multiplying the original PA image (Figure 5a) by the weighting image. The region without magnetic particles is almost completely suppressed, compared to the unchanged regions with MNPs and composite particles.

Similar ideas using magnetic field sensitive particles to quantify and identify particle-labeled pathological regions in US/PA imaging have also been proposed [21–23]. Correlation-based speckle-tracking was applied in US imaging to estimate magnetically induced motion of superparamagnetic iron oxide nanoparticles [21–22], revealing the capability of magnetomotive US imaging in differentiating magnetic nanoparticle-targeted cells from background normal tissues and characterizing the cellular and molecular activity in deep tissues.

The sensitivity of detecting magnetically-induced displacement was also investigated in terms of particle concentration [21] and size (different numbers of precursors forming a cluster) [22]. Liposomes encapsulating gold nanorods and iron oxide nanoparticles were used as the dual contrast agents [23]. In Figure 6, a gelatin phantom mimicking tissue containing six inclusions was imaged using US and PA modalities with magnetic excitation. The region with pure GNRs (i.e., mimicking intrinsic tissue background) is difficult to distinguish from the region with liposomal composite nanoparticles (i.e., mimicking targeted pathological tissues or cells) in the PA image shown in Figure 6b. By estimating displacement induced from the magnetic excitation (Figure 6c) to create a weighting map and multiplying it with the PA image, the region with pure GNRs and background (non inclusion region) can be suppressed (Figure 6d).

3. Potential clinical application: detecting circulating tumor cells

3.1 Detecting CTCs with two targeted contrast agents

In vivo and *in vitro* magnetic trapping of CTCs with two-wavelength PA detection (639 nm and 900 nm) has been demonstrated by targeting both gold-plated carbon nanotubes (GNTs) and MNPs to CTCs, as illustrated in Figure 7 [18]. A cylindrical magnet with field strength of 0.39 Tesla was attached to the region for cell capture. *In vitro* measurements showed that the sensitivity limit was 35 GNTs at 900 nm (peak absorption wavelength of GNTs) and 720 MNPs at 639 nm with a 100 mJ/cm^2 laser fluence. Depletion kinetics tests revealed that the half-life of both particles in mouse circulation was about 15–20 minutes, and cells with pre-labeled contrast agents survived for 60–90 minutes after intravenous injection into a mouse.

CTCs in a murine breast cancer model were magnetically accumulated and detected in subcutaneous vessels. Signal amplitude increased more than 80 times in the abdominal vessels of mice with a tumor at week 2 for a 90 minutes procedure. However, multiple

targeting and multiple wavelength detection increased system complexity. In particular, since it is not easy to find cell surface biomarkers specific to tumor cells, identifying two distinct tumor biomarkers for the same tumor cell is even more difficult.

3.2 Composite contrast agent for detecting CTCs

Panels a and c of Figure 8 present an illustration and a TEM image of composite contrast agents that combine a GNR core with silica coating (Figure 8b) and magnetic nanospheres (MNSs). A GNR has a strong optical response from the visible to near-infrared spectral region (molar absorptivity of 10^9–10^{11} cm^{-1} M^{-1}) [26], and thus an effective contrast agent for generating PA signals. A coated silica shell layer on the GNR improves its photostability and also increases the PA response [27–28]. The absorption spectra of GNR-silica, GNR-silica-MNS, and silica-MNS particles are shown in Figure 8e, which illustrates that the peak absorption wavelength at about 810 nm was unchanged after coating with silica and coupling with MNSs.

3.3 Polystyrene beads mimicking CTCs

Micron-scale polystyrene beads were targeted with GNR-silica-MNS composite particles through carbodiimide hydrochloride (EDC) conjugation reaction to mimic targeted CTCs [24]. A custom magnet system was used to accumulate the targeted beads in a tube with a flow rate of 0.6 ml/min. Figure 9 shows a diagram and photograph of the experimental setup. Two magnets connected to a translation stage can move laterally to trap the beads toward the wall of a tube mimicking a blood vessel. A linear array transducer placed above the tube images the tube region with laser pulses directed from the top.

Figure 10 shows that the PA signals of accumulated beads appear at the left or right side of the tube corresponding to which magnet was closer to the tube, indicating the polystyrene beads with targeted GNR-silica-MNS composites can be trapped by the local magnetic field. Unfortunately, the flow rate in a radial artery is much faster (>6 ml/min) [29], and the trapping force of the two flat magnets is too weak to trap flowing beads at such fast flow rates. Also, paramagnetic MNSs need to be magnetized for effective trapping, and it is difficult to optimize the magnetization field and trapping field at the same time with only a single magnet or pair of magnets.

To trap and manipulate magnetically targeted beads more efficiently, a dual-magnet system was designed and built, as shown in Figure 11 [24]. The set of two flat magnets was preserved and was mainly responsible for providing a homogeneous polarization field. A different magnet array with three cone magnets, which focused a sharp field gradient (>100 m Tesla/mm) inside the tube, was added to generate a strong trapping force on the polarized magnetic particles. The use of two separate sets of magnets for different tasks suggests a robust solution to provide sufficient force to trap and maintain the beads/cells in a fast flowing stream.

Figure 12 shows several representative images of the trapping process for targeted beads in 12 ml/min flow using the dual magnet system. The PA signals in the trapping region increased with time, indicating accumulation of beads trapped by the magnetic force. The signal vanishes after removing the cone magnets due to elimination of the trapping force and wash out of the beads (Figure 12h). At this flow rate, the beads cannot be trapped using only the flat magnets because the flow drag force is too strong. Being able to trap moving beads with the dual magnet system in a flow rate twice that in a human radial artery demonstrates the potential of capturing and detecting CTCs at relatively lower laser fluence (1 mJ/cm^2) compared to Maximum Permissible Exposures [30] in the vasculature with fast blood flow.

Magnetic manipulation of the trapped beads was also demonstrated using the dual magnet system. By moving the cone magnet array along the tube, the cluster of trapped beads moves accordingly (Figure 13 and a video in supporting information) [24]. When moving the cone magnets downstream/left (Figure 13a–c), the trapped beads easily followed the motion. When the cone magnets are moved to the right (upstream, Figure 13d–f), it was harder to follow the motion. The shape of the bead cluster becomes longer due to the downstream drag force of the flow.

Video 1 shows that a fusion movie (US and PA – 20 dB log scale) of magnetic manipulation of trapped beads in 12 ml/min flow [24]. The movie has a different frame rate (frames per second) in different sections: Section 0:00 ~ 3 :00, the magnet moves downflow (to left), 150 frames per second; Section 3:00 to 5:00, magnet stays at −0.5 mm in lateral position, 300 frames per second; Section 5:00 to 12:25, the magnet moves upflow (to right) and then downflow to the middle (−0.2 mm in lateral position), 150 frames per second; Section 12:25 ~ end, release the magnet, 10 frames per second. Note that all fusion images were originally acquired at a 4 Hz frame rate.

Background suppression by magnetically manipulating trapped beads in a highly optically absorptive ink solution with absorption coefficient of 10 cm^{-1} at the irradiating wavelength mimicking blood has also been demonstrated [24]. As presented in Figure 14, the differential image (c) between two images with the cone magnet array at two positions shows that the background was almost completely suppressed but the signals from the trapped beads appearing at the tube bottom wall were preserved. However, residue signals on the top wall arising from the structure of the cone magnet array were also observed in the differential image. They cannot be eliminated using motion filtering because they move coherently with the magnets. This structural artifact limits the contrast improvement in mmPA imaging for this simple magnet configuration. It must be reduced by designing a more robust magnet system that can remotely apply the magnetic field to the region of interest, e.g., an electromagnet based system.

The detection sensitivity, defined as the minimum detectable number of beads (MDB), is roughly estimated as [24]:

$$\mathrm{MDB}=\frac{I_{\mathrm{background}}}{I_{\mathrm{beads}}-I_{\mathrm{background}}}\times N_{\mathrm{beads}}. \quad (1)$$

where $I_{\mathrm{background}}$ is the background signal level, I_{beads} is the integrated signal of accumulated beads, and N_{beads} is the total bead number. Assuming a linear relation between PA signal amplitude and the number of beads, MDB in the system with the dual magnet system at a flow rate of 12 ml/min was estimated as 50 beads [24]. For a reasonable procedure time (e.g., 10 minutes), the screening sensitivity can easily reach fewer than 1 bead/cell per milliliter.

It should be noted that a relatively higher concentration of beads per milliliter solution (1.7×10^6 beads/ml) are imaged in this study (a typical concentration of CTCs in the blood is 1 ~ 10 CTCs/ml) [24].

3.4 HeLa cells as imaging targets

In vitro experiments were also conducted using a human cervical cancer cell line, HeLa, which overexpresses folate receptor (FR). The cell was biochemically labeled with GNR-silica-MNS composites via a targeting ligand, folic acid (FA) [25]. Figure 15 illustrates the structure of the multifunctional composite and its molecular binding to a CTC.

To test targeting specificity and selectivity, several cell samples reacted with different particles, including GNR-silica-FA, silica-MNS-FA, GNR-silica-MNS, and GNR-silica-MNS-FA, were imaged using mmPA imaging with laser fluence of 5.5 mJ/cm^2. Figure 16 shows results of the trapping process at time 4 minutes and 40 seconds after applying the trapping force [25]. The image of cells reacted with GNR-silica-FA (Figure 16a) acts like a traditional PA molecular image. Although the cells can be molecularly targeted with the contrast agent, they cannot be trapped and thus no signals were detected. In contrast, cells reacted with silica-MNS-FA can be magnetically trapped. However, MNSs have lower optical absorption compared to GNRs. Consequently, no signals are seen in the display range, as shown in Figure 16b. For cells with GNR-silica-MNR composite but no FA ligand (Figure 16c), small signals appear in the trapping region due to non-specific binding of the composite to the cells. Finally, the experimental group in Figure 16d, cells with targeted composite, shows much higher PA signals than other samples, indicating that mmPA imaging detects composite contrast agent targeted cells specifically and sensitively.

The solution of GNR-silica-MNP-FA labeled HeLa cells was diluted to 1 cell/ml concentration for trapping measurements. The concentration is at the low end of the typical range of CTCs in the vasculature for an active tumor. Figure 17 depicts several representative images of the 80-minutes trapping process at 6 ml/min flow rate. The first detected signal arises at 34 minutes, meaning the number of trapped cells just exceeds the detection limit. The experiment proceeded for 80 minutes and achieved an overall trapping efficiency of 67% (i.e., percentage of circulating cells that were trapped) [25]. At this efficiency, the total number of cells trapped at 34 minutes is estimated as 136, higher than the MDB mentioned in Section 3.3. Nevertheless, the sample only flows through the trapping region once, similar to *in vivo* conditions within a blood vessel where the contrast agents or the cells can be cleared during every complete circuit. In contrast, a recirculating flow was used for the beads experiments and a free bead can flow through the trapping region over and over again until trapped.

Background suppression by manipulating targeted cells was also demonstrated, as shown in Figure 18. The differential image (Figure 18c) shows the possibility of detecting cells in a strongly absorptive solution with absorption coefficient of 10 cm^{-1}. Clearly, it is nearly impossible to distinguish the cells before subtracting the two images of trapped cells at two different positions (Figure 18a and b). Although a higher concentration of 500 cells/ml was used in this experiment, the result suggests a potential technology to increase the opportunity of ultrasensitive detection of CTCs in the blood pool.

Before moving toward preclinical studies with a small animal model, several *in vitro* studies in a more realistic physical blood flow environment should be performed, including using pulsatile flow instead of constant flow, specificity tests using control cells lines, detection sensitivity tests by measuring mmPA signals as a function of cell number, etc. Also, depletion kinetics and cytotoxicity profiles of the particles in blood should be tested. Besides, the large size of the current magnet system, and the close distance required to apply sufficient force to trap cells, make it hard to translate the current system for *in vivo* and clinical applications. A more robust magnet system for trapping and manipulation is needed to remotely apply magnetic fields to the region of interest.

4. Conclusion

With the use of a composite contrast agent, mmPA imaging can effectively suppress unwanted background from intrinsic biological absorbers, such as melanin, water, fat, and blood, by inducing magnetic motion in contrast agent labeled regions or cells. Ideally, the detection limit due to tissue background in PA molecular imaging can be reduced to the

level of the fundamental thermal noise of the imaging system. Several factors that affect the quality of background suppression must be solved, including motion from breathing and the heart beat, changes of physiologic conditions such as blood oxygenation, blood cell concentration, etc. A potential clinical application of detecting rare CTCs in the vasculature for early diagnosis of cancer metastasis has also been investigated using mmPA imaging. *In vitro* results show that the current system can detect CTCs at a concentration below the typical range found in the vasculature. Using composite contrast agents containing magnetic nanoparticles, a combination of US/PA imaging and magnetic resonance imaging (MRI) can be expected in the near future to significantly impact molecular diagnostics, imaging, and therapeutics.

Acknowledgments

This work was supported in part by NIH RO1EB016034, RO1CA170734, R01CA131797, R01CA140295, T32CA138312, NSF 0645080, the Life Sciences Discovery Fund 3292512, and the Department of Bioengineering at the University of Washington.

References

1. O'Donnell M, Xia J, Pelivanov I, Wei C-W, Hu X, Gao X. SPIE Newsroom. 2012
2. Karabutov AA, Podymova NB, Letok-hov VS. Appl. Phys. B. 1996; 63(6):545–563.
3. Li H, Wang LV. Phys. Med. Biol. 2009; 54(19):R59–R97. [PubMed: 19724102]
4. Larina IV, Larin KV, Esenaliev RO. J. Phys. D: Appl. Phys. 2005; 38(15):2633–2639.
5. Pramanik M, Ku G, Li CH, Wang LV. Med. Phy. 2008; 35(6):2218–2223.
6. Talbert RJ, Holan SH, Viator JA. Phys. Med. Biol. 2007; 52(7):1815–1829. [PubMed: 17374913]
7. Jin X, Li CH, Wang LV. Med. Phys. 2008; 35(7):3205–3214. [PubMed: 18697545]
8. Zerda A, Liu Z, Bodapati S, Teed R, Vaithilin-gam S, Khuri-Yakub BT, Chen X, Dai H, Gambhir SS. Nano Lett. 2010; 10:2168–2172. [PubMed: 20499887]
9. Emelianov SY, Li PC, O'Donnell M. Phys. Today. 2009; 62(5):34–39. [PubMed: 20523758]
10. Li PC, Wang CRC, Shieh DB, Wei CW, Liao CK, Poe C, Jhan S, Ding AA, Wu YN. Opt. Express. 2008; 16(23):18605–18615. [PubMed: 19581946]
11. Weigelt B, Peterse JL, van 't Veer LJ. Nat. Rev. Cancer. 2005; 5:591–602. [PubMed: 16056258]
12. Miller MC, Doyle GV, Terstappen LWMM. J. Oncol. 2010
13. Fleisher M. Clin. Lab. News. 2008; 34
14. Nagrath S, Sequist LV, Maheswaran S, Bell D, Irimia D, Ulkus L, Smith MR, Kwak EL, Digumarthy S, Muzikansky A, Ryan P, Balis UJ, Tompkins RG, Ha AD. Nat. 2007; 450:1235–1239.
15. Zhenga S, Linb H, Liua JQ, Balicb M, Datarb R, Coteb RJ, Tai YC. J. Chromatogr. A. 2007; 1162(2):154–161. [PubMed: 17561026]
16. Shaffer DR, Leversha MA, Danila DC, Lin O, Gonzalez-Espinoza R, Gu B, Anand A, Smith K, Maslak P, Doyle GV, Terstappen LW, Lilja H, Heller G, Fleisher M, Scher HI. Clinical Cancer Research. 2007; 13:2023–2029. [PubMed: 17404082]
17. He W, Wang H, Hartmann LC, Cheng JX, Low PS. Proc. Natl. Acad. Sci. USA. 2007; 104:11760–11765. [PubMed: 17601776]
18. Galanzha EI, Shashkov EV, Kelly T, Kim J-W, Yang L, Zharov VP. Nat. Nanotechnol. 2009; 4:855–860. [PubMed: 19915570]
19. Jin Y, Jia C, Huang S-W, O'Donnell M, Gao X. Nat. Commun. 2010; 1:1. [PubMed: 20975674]
20. Jia C, Huang S-W, Jin Y, Seo CH, Huang L, Eary JF, Gao X, O'Donnell M. Proc. SPIE. 2010:7564–756416.
21. Mehrmohammadi M, Yoon KY, Qu M, Johnston KP, Emelianov SY. Nanotechnol. 2011; 22:045502.
22. Mehrmohammadi M, Oh J, Mallidi S, Emelianov SY. Mol. Imaging. 2011; 10(2):102–110. [PubMed: 21439255]

23. Qu M, Mallidi S, Mehrmohammadi M, Truby R, Homan K, Joshi P, Chen Y-S, Sokolov K, Emelianov SY. Biomed. Opt. Express. 2011; 2(2):385–395. [PubMed: 21339883]
24. Wei C-W, Xia J, Pelivanov I, Hu X, Gao X, O'Donnell M. J. Biomed. Opt. 2012; 17:101517. [PubMed: 23223993]
25. Hu X, Wei C-W, Xia J, Pelivanov I, O'Donnell M, Gao X. Small. 2012
26. Link S, El-Sayed MA. Int. Rev. Phys. Chem. 2000; 19:409–453.
27. Chen L-C, Wei C-W, Souris JS, Cheng S-H, Chen C-T, Yang C-S, Li P-C, Lo L-W. J. Biomed. Opt. 2010; 15:016010. [PubMed: 20210456]
28. Chen Y-S, Frey W, Kim S, Homan K, Kruizinga P, Sokolov K, Emelianov S. Opt. Express. 2010; 18:8867–8877. [PubMed: 20588732]
29. Moore DF, Altarescu G, Pursley R, Campia U, Panza JA, Dimitriadis E, Schiffmann R. BMC Cardiovasc. Disord. 2002; 2(1)
30. A. N. S. Institute. , editor. American National Standard for the Safe Use of Lasers in Health Care Facilities: Standard Z136.1–2000. New York, NY: ANSI, Inc.; 2000. p. 62-66.

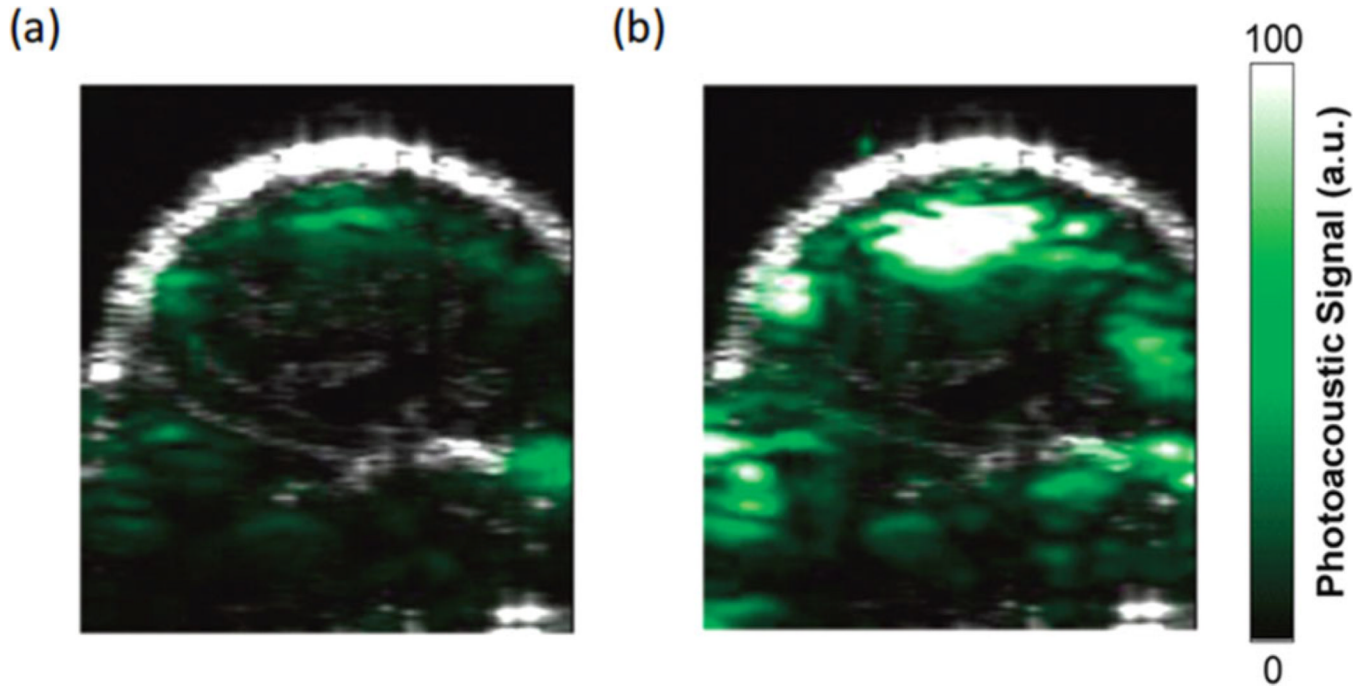

Figure 1.
Photoacoustic molecular imaging of a tumor in a living mouse [8]. Ultrasound (gray) and photoacoustic (green) images of one vertical slice through the tumor. (**a**) Pre-injection image, and (**b**) 2 hours post-injection image of tumor with RGD peptide-coupled carbon nanotubes targeted to $\alpha_v\beta_3$ integrins overexpressed in the tumor vasculature.

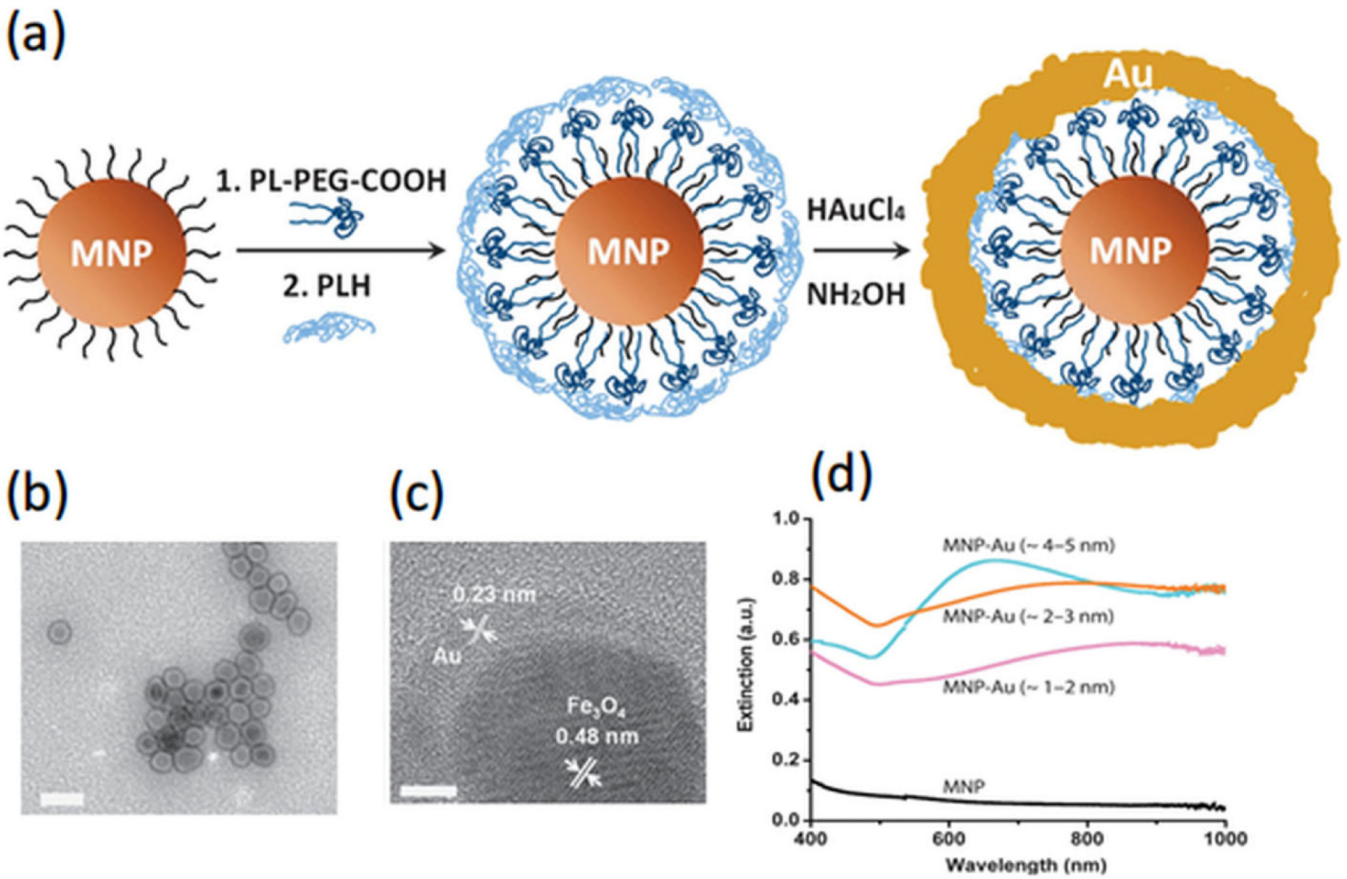

Figure 2.

Schematic, TEM images, and extinction spectrum of MNP-gold core-shell NPs [19]. (**a**) Key steps involved in hybrid NP synthesis (figure not drawn to scale). (**b**) TEM image of MNP-gold core-shell NPs with 2–3 nm shell thickness. Scale bars are 50 nm. (**c**) High-resolution-TEM images of MNP-gold core-shell NPs. The scale bar is 5 nm. (**d**) UV-vis spectra of bare MNPs (black), and with gold nanoshells of various thicknesses: 1–2 nm (purple), 2– 3 nm (orange) and 4–5 nm (blue).

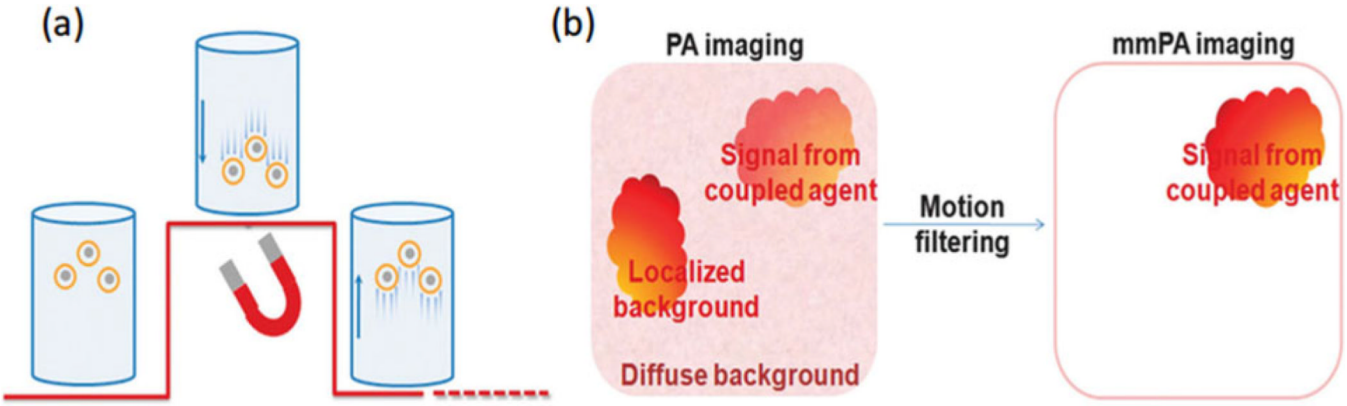

Figure 3.

Schematic of mechanism of background suppression using mmPA [19]. (**a**) Schematic of MNP-gold core-shell NPs' response to a magnetic field. The underlying red curve represents field strength. The coupled agents move as the magnetic field is turned on and off. (**b**) Schematic of contrast enhancement in mmPA imaging, which suppresses regions not susceptible to a controlled magnetic field while identifying regions with coupled agents responsive to a magnetic field.

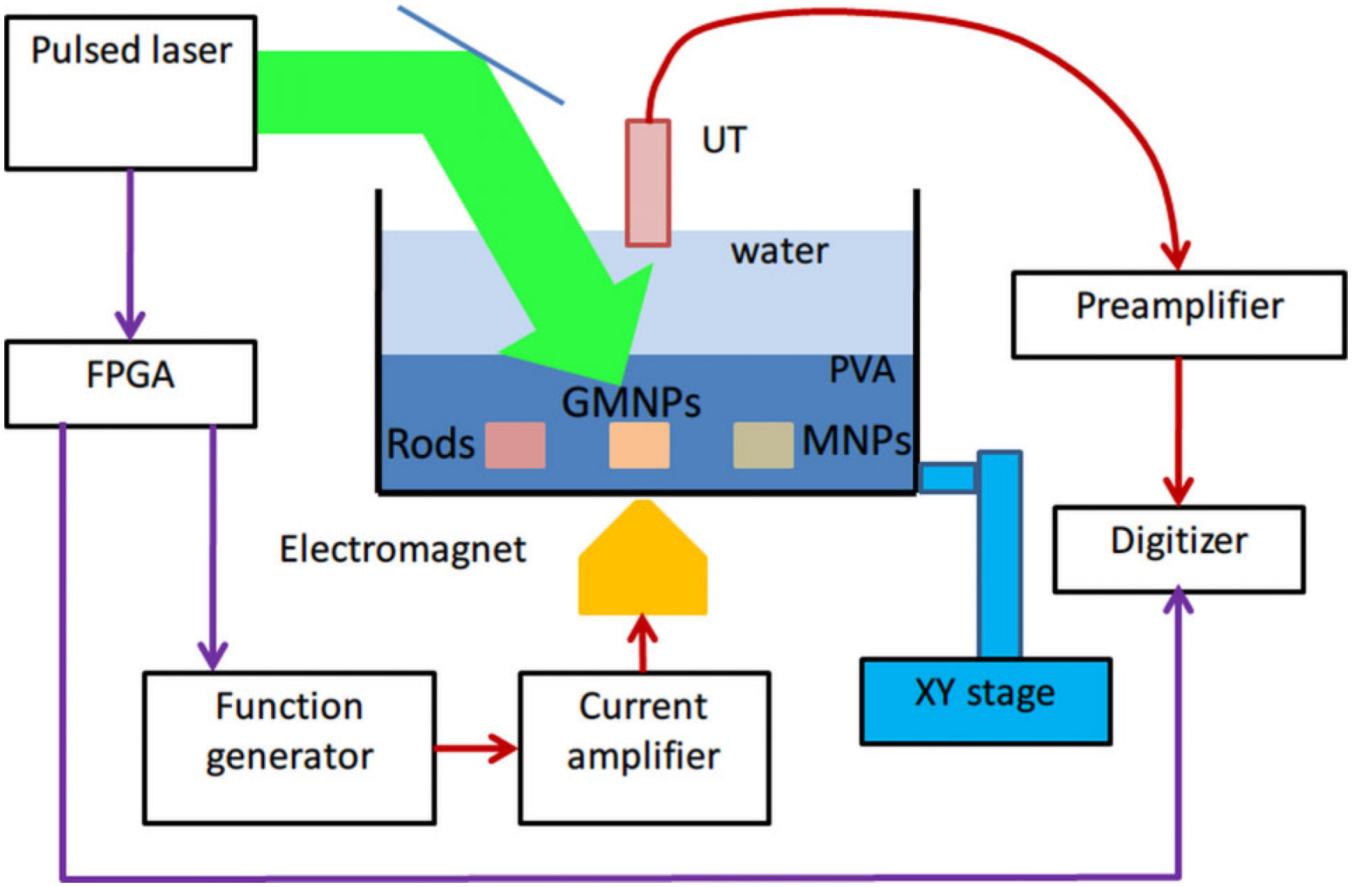

Figure 4.
Schematic of experimental setup of mmPA imaging on a PVA phantom holding three inclusions including gold nanorods, MNP-gold hybrid NPs, and MNPs [20].

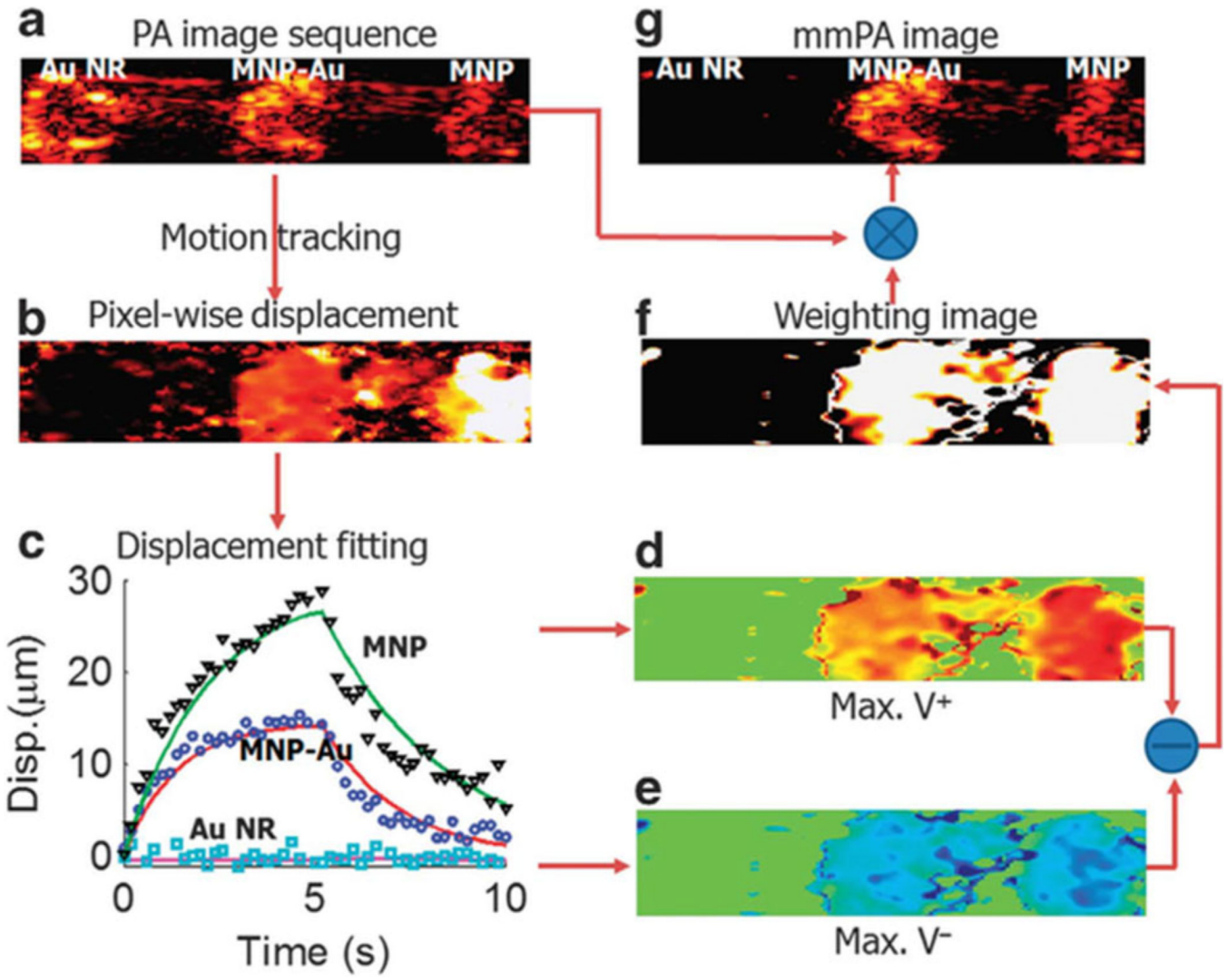

Figure 5.

Data processing in mmPA imaging of MNP-gold hybrid NPs [19]. (**a**) A conventional PA image of the phantom in Figure 4. (**b**) Maximum displacement resulting from the action of the magnetic field presented on a pixel – pixel basis. (**c**) Three representative displacement traces and their fitted curves over the entire time interval of the experiment for pixels in different inclusions. (**d, e**) Velocity computed over the full interval when the magnetic field is turned on and off. (**f**) Weighting image based on the magnitude of the difference between peak positive velocity in the first half and peak negative velocity in the second half. (**g**) mmPA image produced from the product of (**a**) with (**f**).

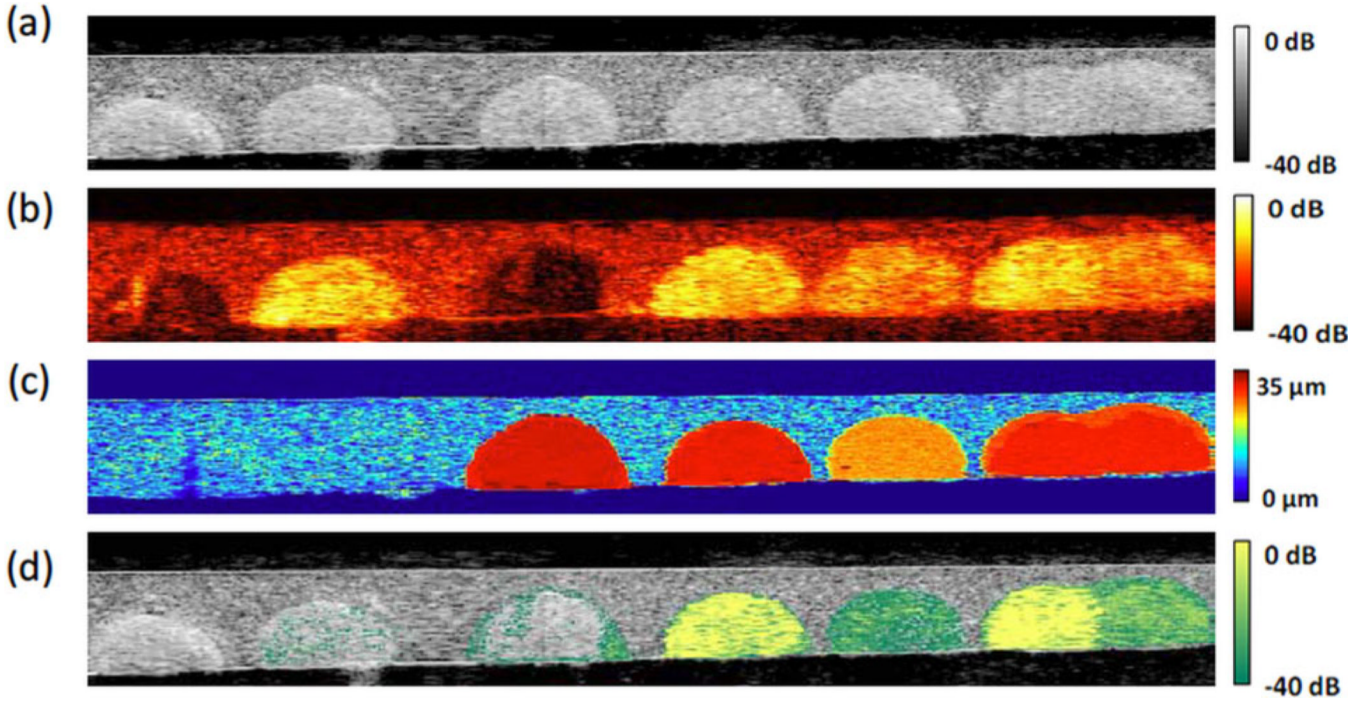

Figure 6.

Images of the tissue-mimicking phantom with different inclusions (left to right): control with gelatin only, 0.70 mg/ml GNRs, 0.60 mg/ml MNPs, high concentration (0.70 mg/ml GNR and 0.60 mg/ml MNP) of liposomal nanoparticles, low concentration (0.47 mg/ml GNR and 0.40 mg/ml MNP) of liposomal nanoparticles, high and low concentration of liposome putting together [23]. (**a**) US image. (**b**) PA image. (**c**) Magneto-motive US image. (**d**) Magneto-photoacoustic image.

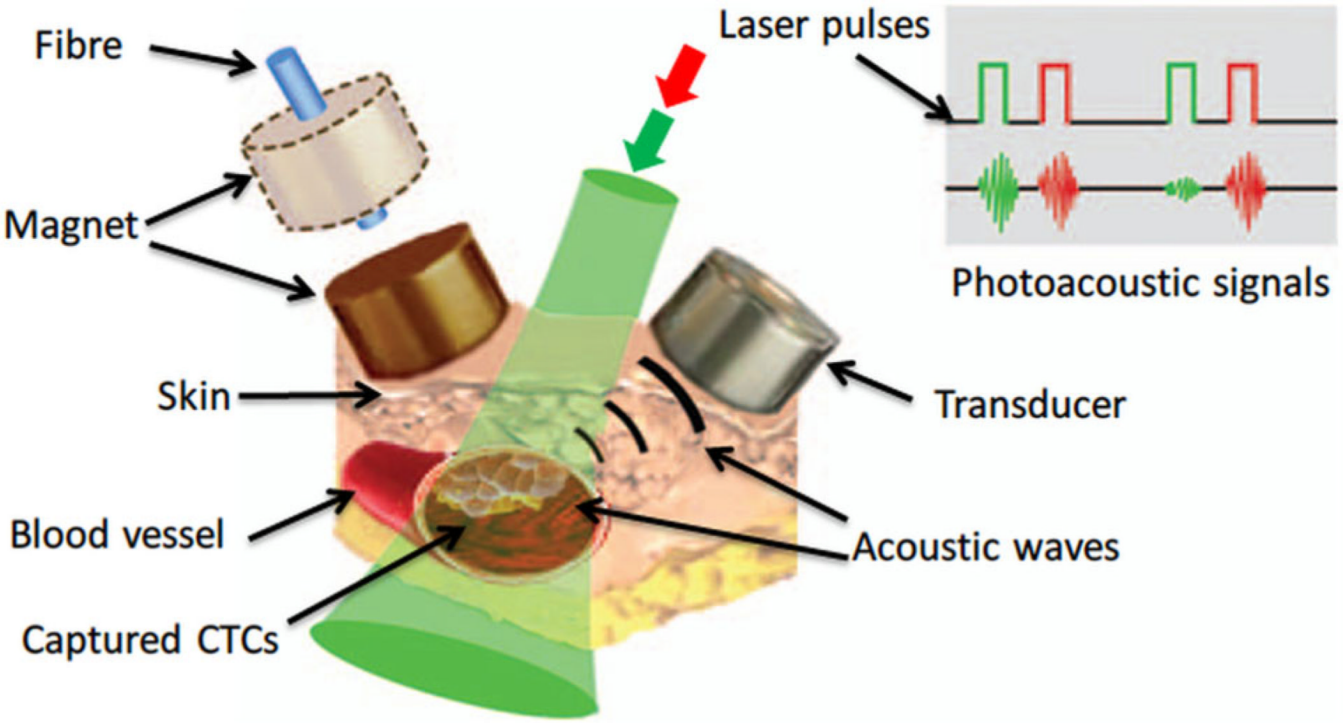

Figure 7.
In vivo magnetic enrichment using two-color PA detection of CTCs with multiple targeted contrast agents: MNPs and GNTs [18].

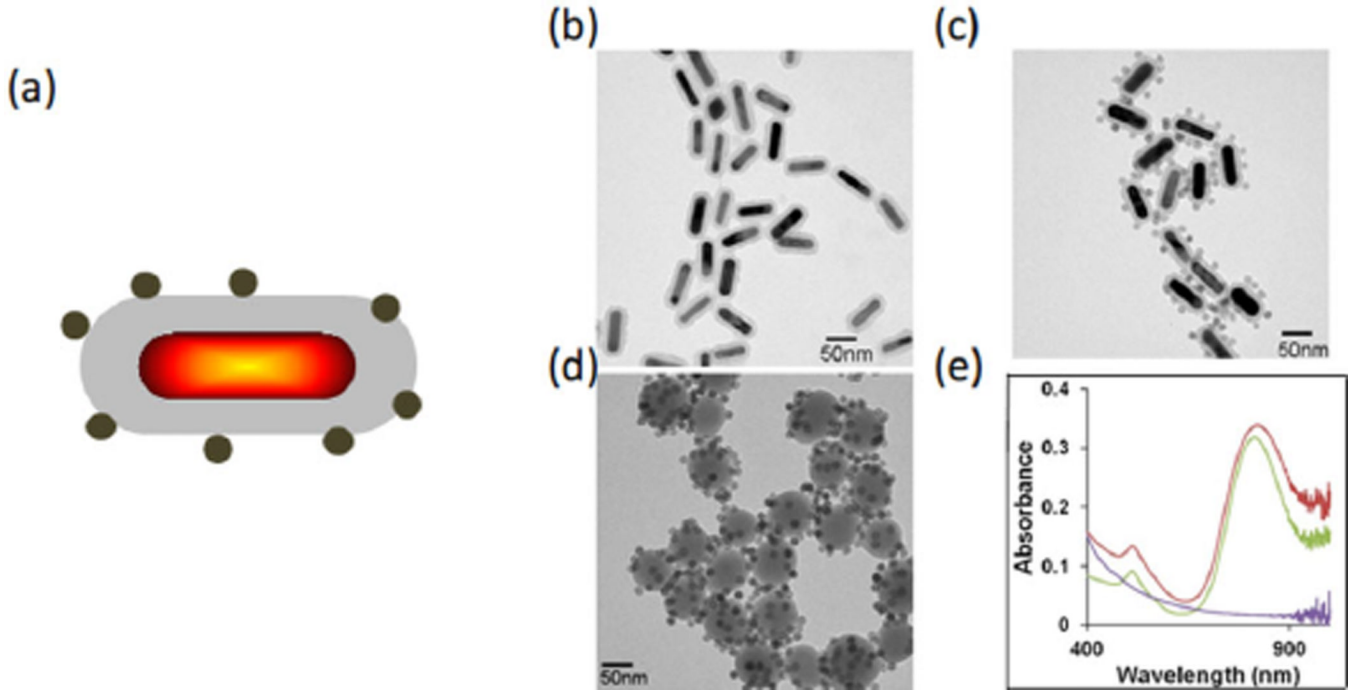

Figure 8.

Characterization of GNR-MNS composites [25]. (**a**) Schematic illustration of the multifunctional nanoparticle. (**b–d**) TEM images of GNR-silica, GNR-silica-MNS, and silica-MNS particles (scale bars: 50 nm). (**e**) Corresponding ultraviolet-visible spectra of the three samples. The silica-MNS particles exhibit a decaying absorption profile from 400–1000 nm (purple), and the silica-encapsulated GNR shows a characteristic longitudinal surface plasmon resonance (SPR) peak at 812 nm (green). After MNS conjugation, the longitudinal SPR peak slightly red-shifts to 827 nm, and absorption at the ultraviolet range is significantly elevated due to contributions from the MNSs (red).

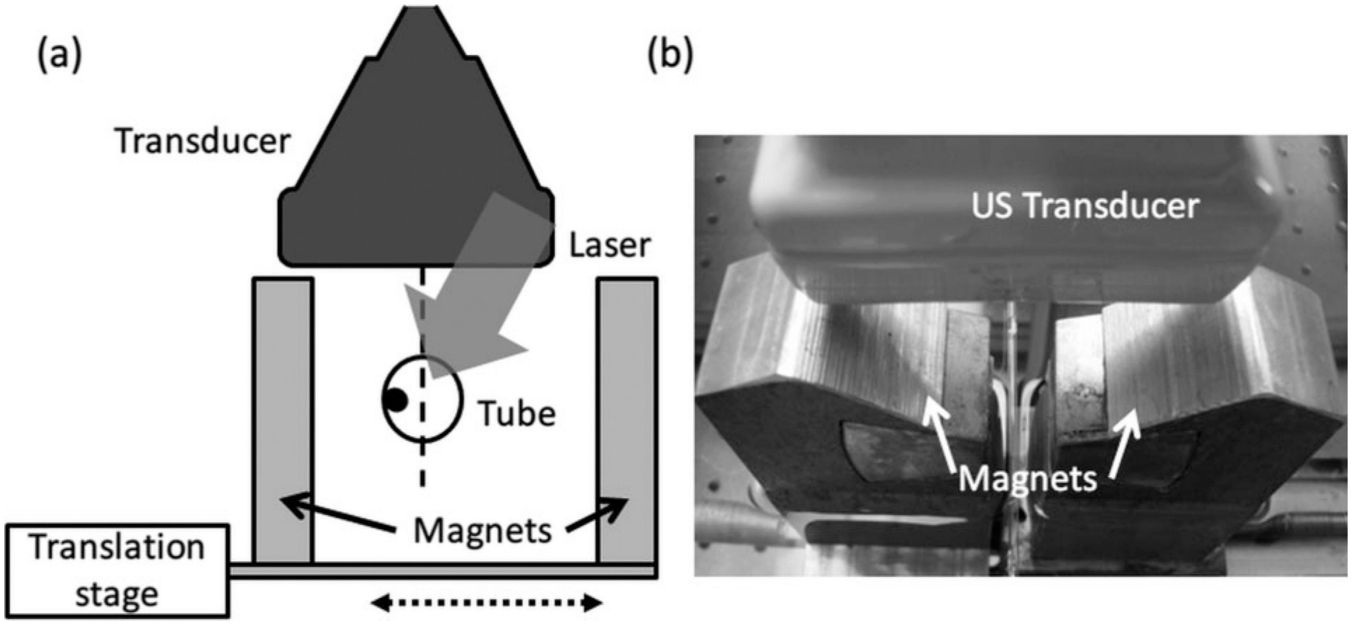

Figure 9.

(**a**) Diagram and (**b**) photograph of experimental setup showing magnetic trapping and manipulation of polystyrene beads targeted with composite nanoparticles. The setup includes a flow tube, magnets for manipulation, incident-laser, and a linear array US imaging transducer.

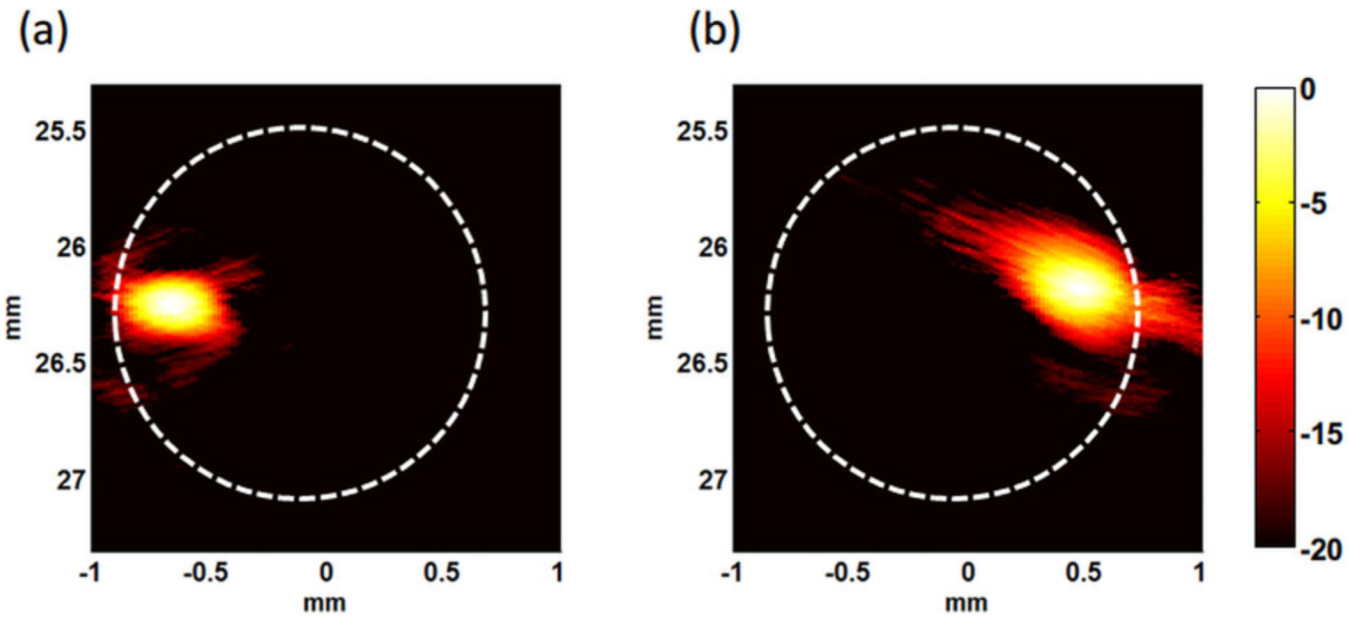

Figure 10.
PA images displayed on a logarithmic scale (20 dB) of polystyrene beads trapped in 0.6 ml/min flow with (**a**) tube closer to the left magnet, and (**b**) tube closer to the right magnet. Dashed circles indicate the tube.

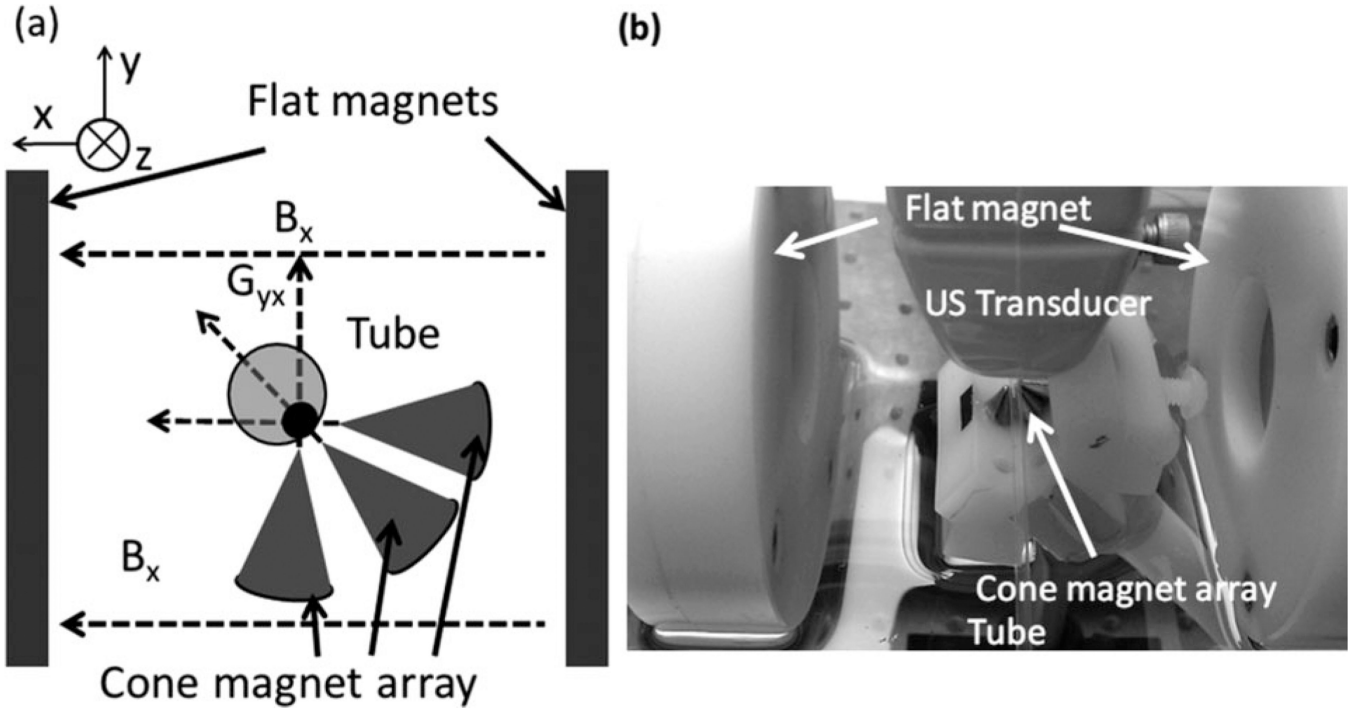

Figure 11.

(**a**) Diagram and (**b**) photograph of dual-magnet system [24]. The system consists of a pair of flat magnets providing the polarization field, and a cone magnet array providing a strong trapping force.

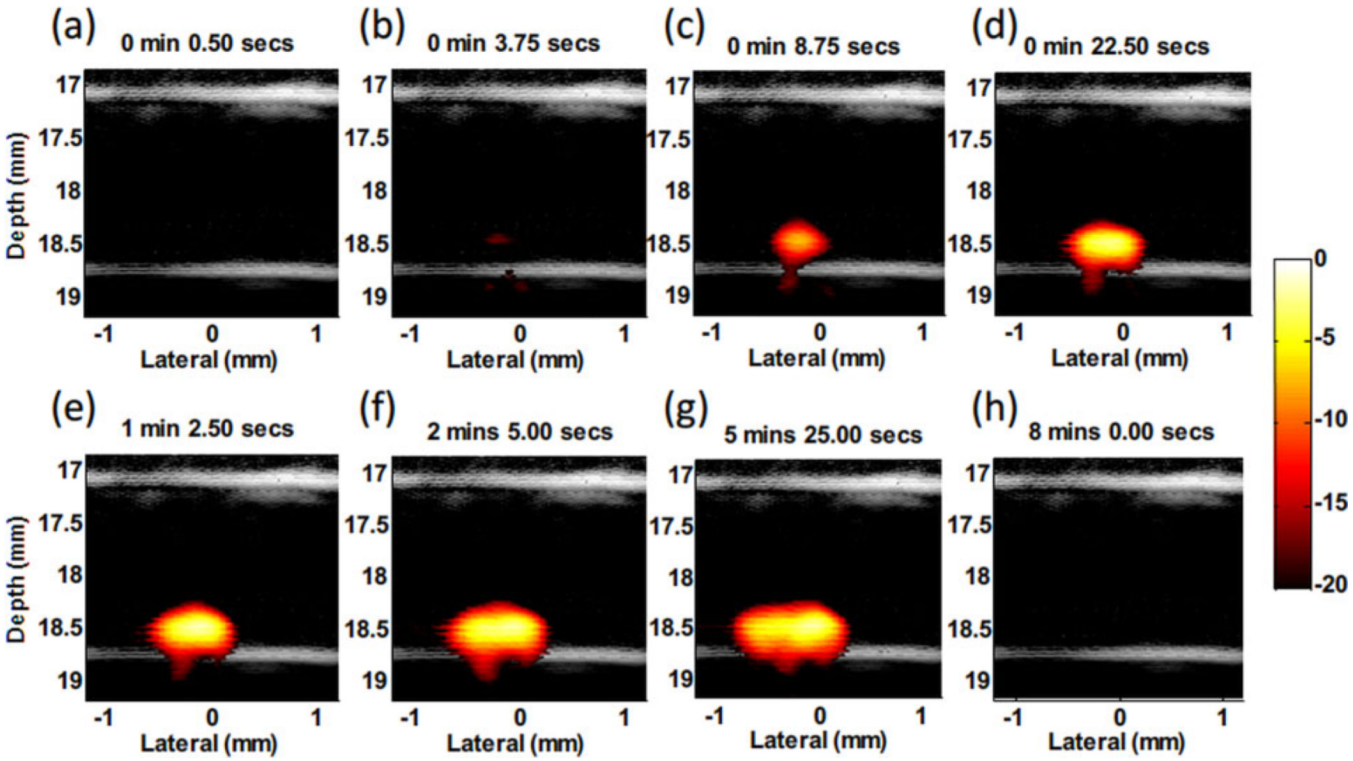

Figure 12.

Fusion images (US and PA – 20 dB log scale) of magnetic trapping of beads targeted with composite particles at different time points of magnet action [24]. The beads travel in a 12 ml/min flow stream. (**a**) Right after applying magnetic trapping force. (**b–g**) Accumulating targeted beads. (**h**) Release of beads by removing magnetic trapping force.

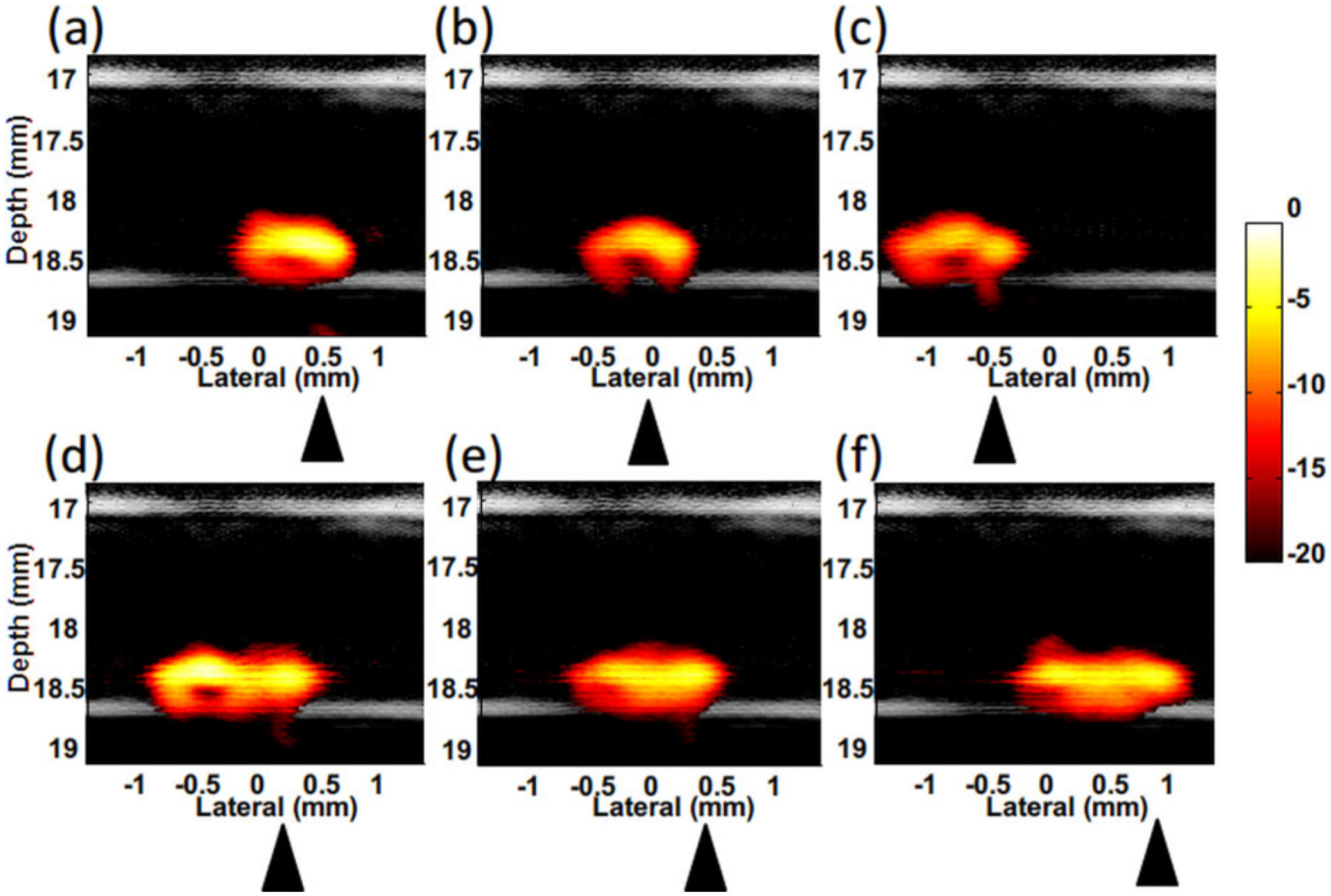

Figure 13.

Fusion (US and PA – 20 dB log scale) images of magnetic manipulation of trapped polystyrene beads in the flow stream with flow rate of 12 ml/min [24]. (**a**–**c**) Move the magnet to left (downstream). (**d**–**f**) Move the magnet to right (upstream). Triangles indicate the magnet position.

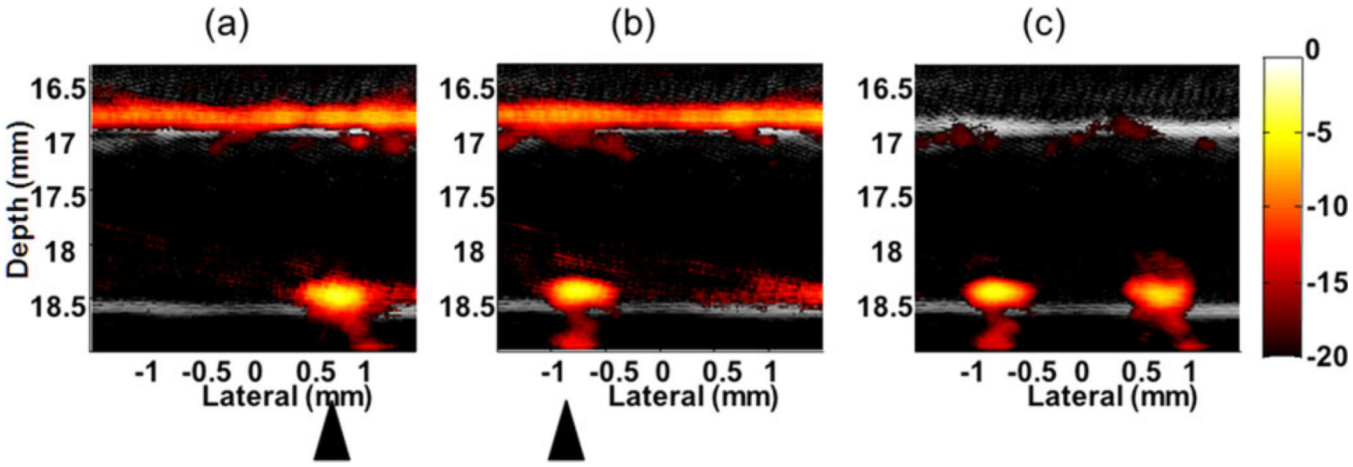

Figure 14.

Background suppression by manipulating targeted beads in ink solution (absorption coefficient of 10 cm^{-1}) with 12 ml/min flow stream [24]. Images (**a**) and (**b**) acquired at two different positions of the cone magnet array. (**c**) Differential image of (**a**) and (**b**). Triangles indicate the magnet positions. (20 dB log scale)

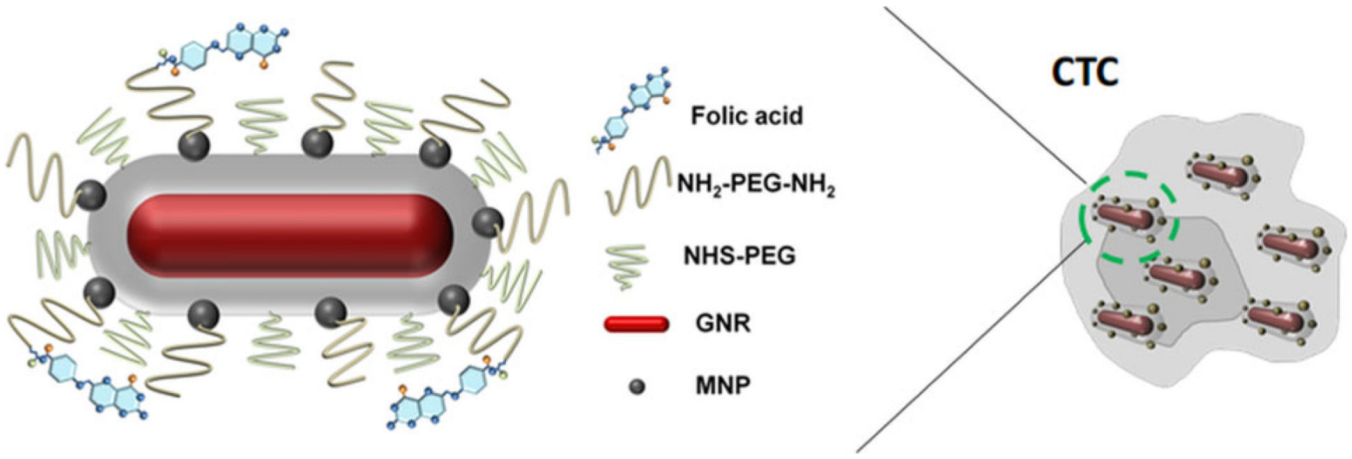

Figure 15.

Composite contrast agent molecularly targeted to a CTC [25]. GNRs with desired aspect ratio not only provide strong near-infrared absorbance, but also serve as a structural scaffold for silica shell growth and attachment of MNSs. Polyethylene glycol (PEG) chains with a terminal reactive site are grafted onto the multifunctional nanoparticle, and FA as a model targeting ligand is linked to the particles through PEG.

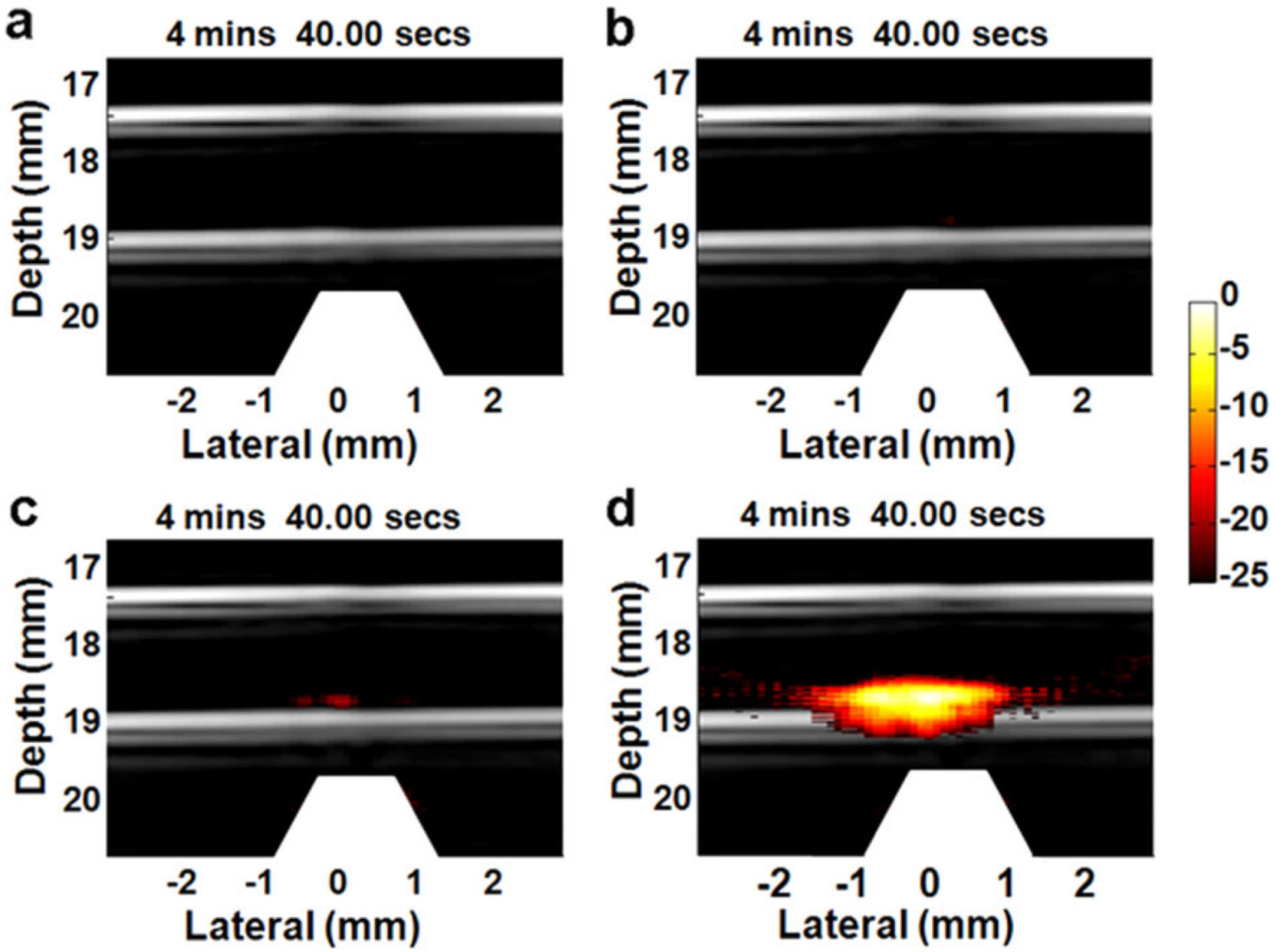

Figure 16.

Fusion images (US and PA – 25 dB log scale) of captured HeLa cells [25]. The cells are labeled with (**a**) GNR-silica-FA, (**b**) silica-MNS-FA, (**c**) GNR-silica-MNS, and (**d**) GNR-silica-MNS-FA, and infused into the circulation system at a concentration of 5,000 cells/ml. The images shown are selected at the same time point (4: 40) after applying the magnetic trapping force. The trapezoids appearing below the tube indicate the magnets. When targeted by FA (**d**), the total PA signals are more than 20 dB higher than the non-targeted control (**c**).

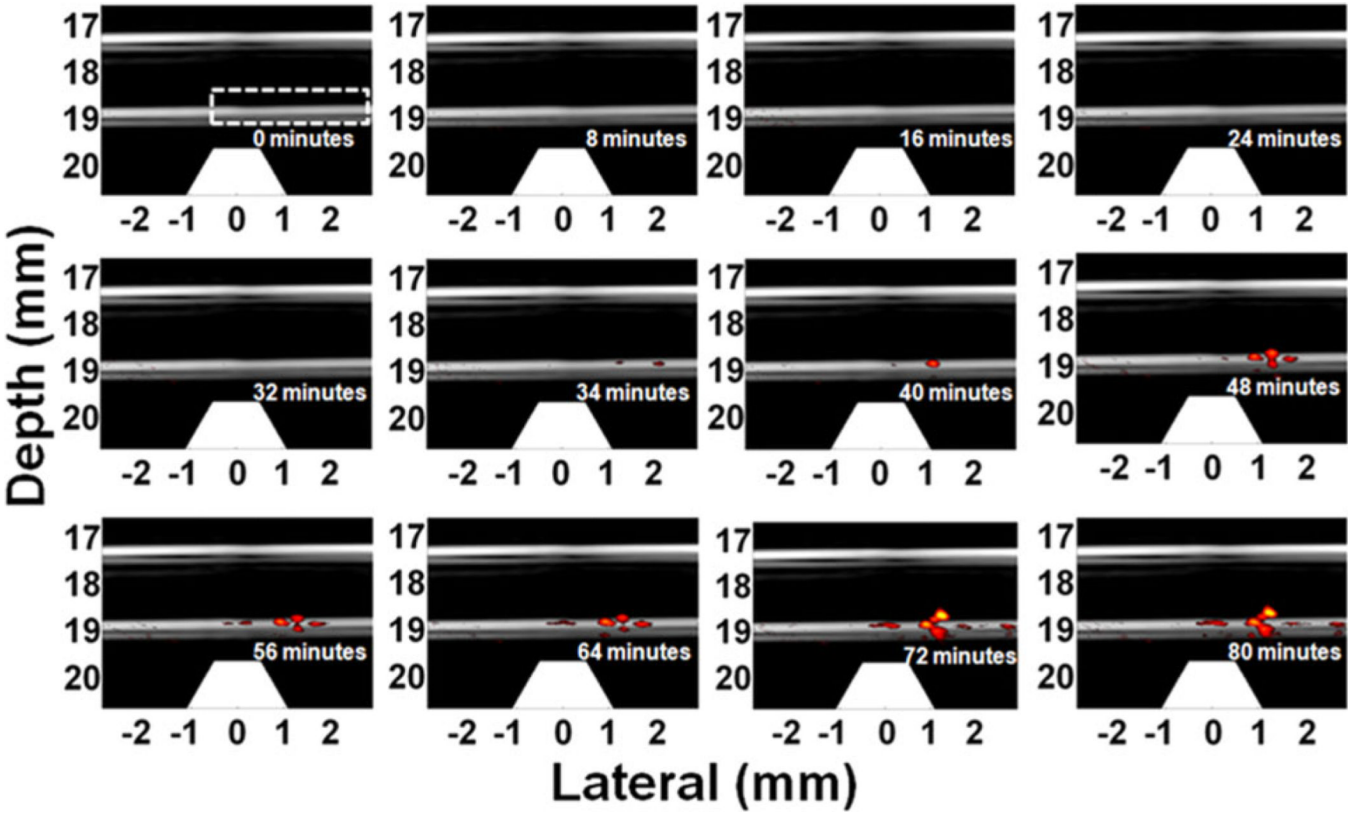

Figure 17.
Twelve representative time-lapse US/PA images (20 dB log scale) of the trapped GNR-silica-MNS-FA labeled HeLa cells at 1 cell/ml concentration [25]. First detectable PA signal appears at 34 minutes, and the signal increases afterward, indicating cell accumulation. Trapezoids indicate the magnets.

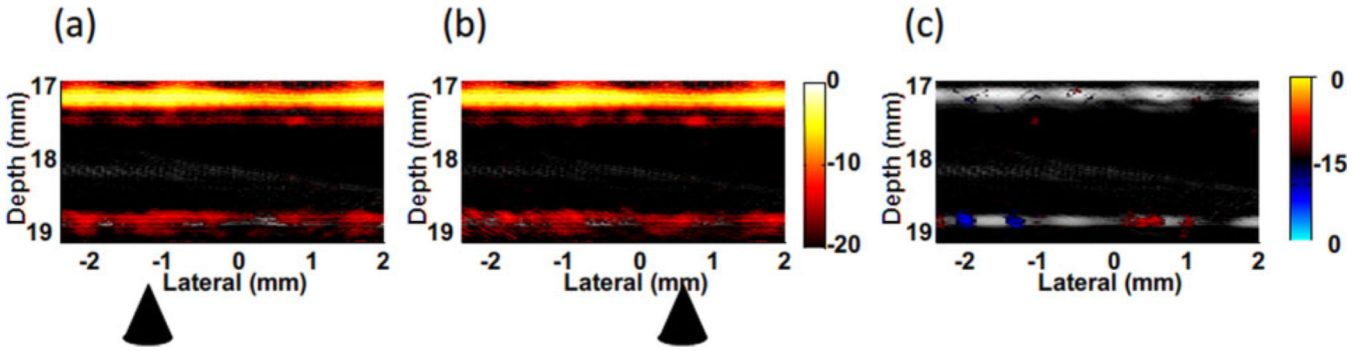

Figure 18.

Background suppression by manipulating targeted cells in ink solution with 6 ml/min flow stream. The cell concentration is 500 cells/ml solution. Images (**a**) and (**b**) acquired for two different positions of the cone magnet array. (**c**) Differential image (bipolar, 15 dB log scale) of (**a**) and (**b**). Triangles indicate the magnet positions.